Pergamon

Int. J. Heat Mass Transfer. Vol. 38, No. 12, pp. 2281–2295, 1995

0017-9310/95 $9.50+0.00

0017–9310(94)00336–X

Calculation of meniscus shapes and transport processes in float zone

WEI SHYY and MADHUKAR M. RAO

Department of Aerospace Engineering, Mechanics and Engineering Science, University of Florida, Gainesville, FL 32611, U.S.A.

(*Received* 16 *March* 1994 *and in final form* 5 *October* 1994)

Abstract—The formation of the melt meniscus and convection heat transfer in the melt is a major issue in the float zone technique for growing single crystals. The present study investigates the issues of existence, multiplicity and physical realizability of the solutions, based on the concept of free energy minimization, to the Young–Laplace equation, representing the liquid menisci formed under equilibrium conditions. The physical realizability of the meniscus profile is sharply affected by the material properties and geometry, through the dimensionless parameters including Bond number and aspect ratio. A typical meniscus shape obtained at Bond numbers commonly encountered in practical configurations is selected for buoyancy driven convection and thermocapillary convection heat transfer studies. For the materials and geometries of interest, thermocapillary effects dominate over buoyancy effects. The impact of the convection pattern on the meniscus shape is reflected by the magnitude of the capillary number, which is found to be small in this case. Calculations were conducted over a range of Grashof numbers, Marangoni numbers and Prandtl numbers to gage the sensitivity of the solutions to the physical properties of the molten material. The relative strength of buoyancy-driven convection and thermocapillary convection has the greatest impact on the heat transfer results. The results reported here can help assess the suitability of a given float zone design.

1. INTRODUCTION

The float zone technique is one of the candidate methods for growing single crystals. The main advantage of the float zone process is that it is a containerless process and contamination from the wall, a main source of problems for crystal quality control, is removed. On Earth, it is mainly limited by the size of the melt zone that can be achieved, since the hydrostatic pressure of the melt zone and the normal stresses induced by flow motion is balanced by the surface tension between the melt and the ambient fluid. Another problem is the loss of volatile components from the melt, which can be circumvented by the use of encapsulating liquids. The encapsulant can also increase the maximum size of the melt zone that can be achieved by reducing the hydrostatic pressure difference between the melt and its surroundings. The objective of this study is to investigate the generation of meniscus shapes for floating zone configurations. The formation of the meniscus during the melting process is a major concern in the successful operation of the float zone technique. This aspect and associated transport processes will be the focus of the present work. Specifically, the issues of existence, multiplicity and sensitivity of solutions to the Young–Laplace equation representing the liquid meniscus formed under equilibrium conditions, will be investigated based on a free energy concept originated by Shyy *et al* [1]. The approach is static in nature, which is a satisfactory approximation considering the slow speed of the movement of the melt typical of most practical applications. Although the static consideration cannot account for the dynamics of the interface characteristics, in general, the slow growth rates of many crystal processing techniques allow meaningful application of this theoretical framework. Figure 1(a) is a schematic illustration of the float zone process and Fig. 1(b) is a schematic of the mathematical model employed in the present model, which allows, as it should, the trijunction point to move to satisfy a given value of the static contact angle or other constraints, such as a fixed volume of the melt.

With the theoretical and computational framework of determining the meniscus shape in place, this work then addresses the issues of thermal transport in the melt. Specifically, the role of buoyancy induced convection, Marangoni convection and their mutual interaction affecting thermal transport, excluding phase change aspects, will be elucidated in this work. Extensive investigations of high Marangoni number thermocapillary convection in a square cavity have been carried out by Zebib *et al.* [3], Carpenter and Homsy [4, 5], combined buoyant and thermocapillary flow in a square cavity by Carpenter and Homsy [4] and impact of thermocapillary convection on the free surface shape by Zebib *et al.* [3]. Shyy and Chen [6] have discussed the interaction of buoyancy and surface tension-driven convection in a rectangular enclosure. They discussed the impact of Prandtl number and the Marangoni number on the convection and heat transfer characteristics in molten alloy. A similar

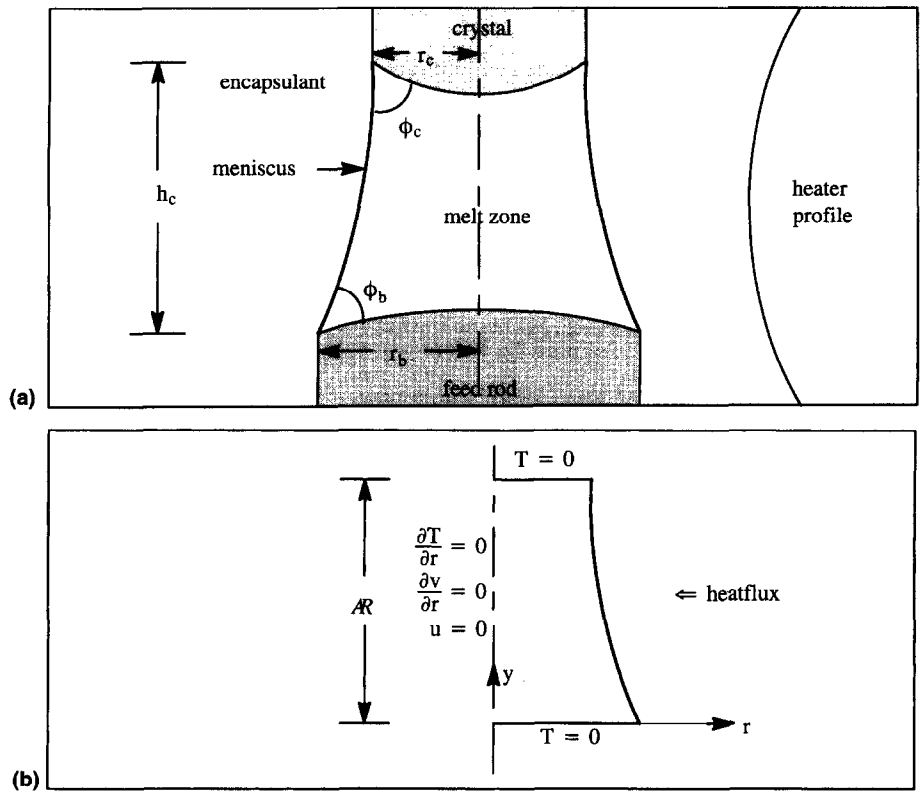

Fig. 1. Schematic of the float zone process and the mathematical model employed. (a). Schematic of the float zone process. The melt zone is sustained by the surface tension between the melt and the encapsulant. The heating profile is schematically illustrated on the right. Axisymmetry has been assumed. (b) Schematic of the mathematical model and geometry employed in the calculation procedure.

study involving the interaction of thermocapillary and natural convection along with phase change effects under both normal and reduced gravity conditions is discussed in Shyy and Chen [7]. A study involving both thermal transport and solute transport is presented by Shyy and Chen [8], which also discusses the effect of complex geometry in the form of a curved boundary.

Some of the earlier works in the numerical modeling of the float zone included thermocapillary convection with a highly simplified cylindrical geometry [9–11]. More complex geometries involving deformable free surfaces have been considered by Murthy [12], Lie *et al.* [13], Neitzel *et al.* [14], Li *et al.* [15], Li and Saghir [16], Zhang and Alexander [17] and others. In ref. [17], the contact lines are fixed and the free surface shape is calculated by iteratively satisfying the governing equations and the volume constraint using a Picard type of iterative procedure. However, in refs. [13, 15], the meniscus contact angles are adjusted to iteratively satisfy the governing equations and the volume constraint. This work considers the interaction of buoyancy-induced and thermocapillary convection in thermal transport in a cylindrical geometry defined by a deformable meniscus. Parameter ranges and material properties directly applicable to an experimental configuration employed for float zone growth of single crystals [18] have been considered, unlike the previous studies. In this study, particular care has been taken to obtain accurate solutions by using second-order centered discretizations and fine grids, unlike the above-mentioned studies. Also, the existence and uniqueness of the meniscus profiles have been discussed, which is an issue that has not been treated in previous studies. For simplicity, this study is restricted to convective thermal transport only. Considerations of solute transport and phase change will be addressed subsequently. While the shape of the phase boundary between the melt and the solid can affect the detailed transport processes, especially for low Prandtl number materials [8, also 2, p. 448], the information gathered from the present effort can serve as a basis for that extension.

2. PREDICTION OF MENISCUS SHAPES

2.1. *Methodology*

Meniscus profiles obey the Young–Laplace equation in axisymmetric form [2, 19, 20], which relates the

curvature of the free surface to the pressure difference across it. The governing equation describes the generation of surface curvature to balance the sum of the hydrostatic pressure and pressurization. Specialized to an axisymmetric geometry and isothermal domain without melt convection, it can be written as follows:

$$\Delta\rho g\, y - \Delta P = \sigma\left[\frac{f''}{(1+f'^2)^{3/2}} - \frac{1}{f(1+f'^2)^{1/2}}\right] \quad (1a)$$

where $\Delta\rho$ is the density difference between the ambient and the melt and ΔP is the pressurization. σ is the surface tension coefficient and the meniscus is described by $f = r(y)$, where r is the radius and y is the vertical coordinate. A variety of boundary conditions have been treated in literature, such as fixed contact angles at both top and bottom [19–21], fixed radius at the bottom and fixed contact angle at the top [1] and fixed radius at both top and bottom [10–12, 15, 17, 22]. These conditions have been devised for configurations under different physical constraints. In the context of floating zones, the boundary conditions to be imposed may vary depending on the operating conditions. Therefore this study has been conducted with a variety of different constraints imposed on the solutions. The following boundary conditions may be imposed:

$$f(y = 0) = r_b \quad (1b)$$

either

$$f(y = h_c) = r_c \quad (1c)$$

or

$$f'(y = h_c) = \tan(\pi/2 - \phi_c). \quad (1d)$$

Figure 1(b) shows a schematic of the geometry. For an isothermal liquid bridge, equation (1a) can be non-dimensionalized with a length scale of r_b and a pressure scale of σ/r_b, to yield,

$$Bo\, y - \Delta P = \left[\frac{f''}{(1+f'^2)^{3/2}} - \frac{1}{f(1+f'^2)^{1/2}}\right] \quad (2)$$

where the italics indicate non-dimensionalized quantities. *Bo* is the Bond number defined as:

$$Bo = \frac{\Delta\rho g r_b^2}{\sigma}. \quad (3)$$

In ref. [1], the non-linear differential equation (2) was solved subject to a fixed radius at the lower boundary and a fixed contact angle at the top boundary. Such a two-point boundary value problem does not yield a unique solution. Thus there arises the problem of selecting, out of the multiple solutions that are mathematically permissible, the one that corresponds to the physical equilibrium condition that exists in reality. Therefore we now invoke the thermodynamic condition that at equilibrium the free energy is a minimum and select the solution that minimizes the free energy.

For simplicity, we consider only the isothermal condition and examine the Helmholtz free energy, which contains three contributions:

(i) the potential energy from the effective head;

(ii) the surface energy of the meniscus forming the gas–liquid interface;

(iii) the surface energy needed to wet the solid–liquid wetted area.

The equilibrium shape is the one that minimizes the total free energy:

$$E = \int_0^{h_c} [\pi f^2(\Delta\rho g\, y - \Delta P) + 2\pi\sigma f(1+f'^2)^{1/2}]\, dy - \pi\sigma r_c^2 \cos(\phi_0) \quad (4)$$

where ϕ_0 is the static contact angle. The Young–Laplace equation may be integrated, starting with a fixed radius and base angles, $-\pi/2 < \phi_b < \pi/2$, to yield all possible solutions for a given aspect ratio of the domain. Subsequently, solutions satisfying a given contact angle at the top, ϕ_c, are selected and their free energies calculated according to equation (4). If any of these solutions locally minimize the free energy, then these profile shapes are statically stable.

As described in refs. [1, 2], the value of ϕ_0 is specified, and E is calculated by fixing the value of ϕ_0 in equation (4) and scanning through the whole range of meniscus profiles obtained by fixing the lower trijunction location (with varying angle) and the height of the upper trijunction point (with varying locations and angles), distinct extrema are obtained at specified values of ϕ_0. Among the multiple solutions, the one corresponding to a point of minimum on the curve is the physically realizable stable meniscus profile. When either a maximum or a non-extremum point arises, we may surmise that such solutions belong to the unstable branch.

The volume of the melt zone in non-dimensional form is given by,

$$V = \int_0^{AR} \pi f^2\, dy \quad (5)$$

where $AR = h_c/r_b$ is the aspect ratio of the zone. The aim was to determine the sensitivity of the profile shapes to the imposed boundary conditions. In float zones, the meniscus profiles may be required to enclose a fixed volume of the melt, thus satisfying equation (5) [15, 17, 19, 20, 22]. As will be demonstrated, the basic considerations from free energy and uniqueness can shed useful light on the issues relevant to the float zone. It is also noted that additional forces may be generated on the free surface due to electromagnetic effects if the zone is heated by an induction coil [13, 23].

2.2. *Effect of convection on meniscus shape*

It may be expected that convection in the melt will impact the meniscus shape through the normal stress terms, which will be balanced by the free surface cur-

vature. In addition, the free surface will no longer be an isotherm, which implies that the surface tension will vary from point to point, reflecting the spatial distribution of the temperature along the free surface. Equation (1a) must be modified as follows:

$$\Delta\rho g y-\Delta P+2\mu\frac{\partial V_n}{\partial n}=\sigma(T)\left[\frac{f''}{(1+f'^2)^{3/2}}-\frac{1}{f(1+f'^2)^{1/2}}\right] \quad (6)$$

where μ is the viscosity of the melt. This can be non-dimensionalized in a manner similar to equation (1a), along with the reference velocity scale defined as α/r_b, where α is the thermal diffusivity. In non-dimensional form, this becomes:

$$Bo\, y-\Delta P+Ca\frac{\partial V_n}{\partial n}=\left(1-\left|\frac{d\sigma}{dT}\right|\frac{\Delta T}{\sigma_o}\right)\left[\frac{f''}{(1+f'^2)^{3/2}}-\frac{1}{f(1+f'^2)^{1/2}}\right] \quad (7)$$

where Ca is the capillary number defined as $2\mu\alpha/\sigma_o r_b$, where α is the thermal diffusivity, σ_o is the surface tension at the reference temperature and the italics denote the non-dimensionalized variables. The capillary number and the Bond number determine the relative influence of the hydrostatic and the convective effects, respectively. The term premultiplying the curvature term describes the correction due to the variation of surface tension with temperature. In this study, as will be presented later, it is found that the capillary number, Ca, and the normal gradient of the normal velocity are both small compared to the hydrostatic term, from an *a posteriori* estimation, and hence meniscus shapes are generated based on equation (1a).

Only the steady state has been considered in this study. Dynamic effects have been considered by several investigators [24–26]. Quasi-equilibrium studies involving contact angle hysterisis have been treated in refs. [1, 2]. It is considered that the phenomenon of contact angle hysteresis is largely due to surface roughness [27] and surface inhomogeneity [2]. In the present study, it is considered that the melt zone moves slowly and a static consideration suffices.

3. FORMULATION AND COMPUTATIONAL ALGORITHM FOR TRANSPORT PROCESSES

The most influential process variables governing the crystal growth process are the heat and solute transport processes in the melt, which directly impact the shape and movement of the solid–liquid interface at the solidifying front. In the following section, a meniscus configuration frequently encountered in practical float zone processes is isolated for detailed analysis of the heat transport within the melt. Of particular interest in the following study is the role of buoyancy driven and thermocapillary convection processes and the mutual interaction of the convection processes with the shape of the free surface in determining the heat transfer within the melt. Phase change and solute transport effects are deferred to a future study.

The Navier–Stokes equations along with the energy equation are written in cylindrical coordinates to facilitate the treatment of the axisymmetric geometry shown in Fig. 1(b). The numerical scheme involves the discretization of the transformed form of the governing equations based on a control volume formulation as described in refs. [2, 32, 33]. The relevant aspects of this procedure are described below.

An appropriate choice of scales for the non-dimensionalization procedure was arrived at by selecting the base radius, r_b, as the characteristic length scale and the characteristic velocity scale was based on the thermal diffusion velocity scale defined as α/r_b, where α is the thermal diffusivity defined as $k/\rho C_p$. The selection of the temperature scale is not as straightforward, since the boundary condition at the free surface is specified as a heat flux from which an estimate of the maximum temperature in the domain has to be derived. The procedure is explained below in detail.

It is noted that, since heat flux is specified on the free surface, a temperature scale has to be derived in order to non-dimensionalize the energy equation and define the Grashof and the Marangoni numbers. It would seem natural to define a temperature scale based on the heat flux as follows:

$$\Delta T=\frac{q_{max}}{k}d \quad (8a)$$

where q_{max} is the maximum value of the heat flux specified on the boundary. However, it was noted that such a definition overestimated the temperature scale, i.e. the maximum temperature achieved in the domain, even for the conduction case, was at least five times less than the value suggested by equation (8a). It was expected that the maximum temperatures obtained by taking convection into account would be even less. Therefore the temperature scale obtained above was scaled down by a factor of 10 in order to obtain a more realistic temperature scale. Therefore the temperature scale used to calculate the Grashof and Marangoni numbers is:

$$\Delta T=0.1\times\frac{q_{max}}{k}d. \quad (8b)$$

As to the convection mechanisms, the buoyancy effect within the melt and the thermocapillary effect on the free surface have been included in this model. The strength of buoyancy induced convection is indicated by the Rayleigh number defined as

$$Ra=Gr\cdot Pr \quad (9a)$$

where Gr is the Grashof number defined as

$$Gr = \frac{g r_b^3 \Delta\rho}{\nu^2 \rho}. \quad (9b)$$

Invoking the Boussinnesq approximation, this becomes

$$Gr = \frac{g\beta\Delta T r_b^3}{\nu^2} \quad (9c)$$

and Pr is the Prandtl number defined as

$$Pr = \frac{C_p \mu}{k}. \quad (9d)$$

The relative magnitude of the thermocapillary effect is described by the Marangoni number,

$$Ma = \frac{\left|\frac{d\sigma}{dT}\right| \Delta T r_b}{\mu\alpha} \quad (10)$$

where $d\sigma/dT$ describes the variation of the surface tension with the temperature.

The governing equations may be non-dimensionalized with respect to the reference scales described at the start of this section, as follows:

(i) continuity

$$\frac{\partial(ru)}{\partial r} + \frac{\partial(rv)}{\partial y} = 0 \quad (11a)$$

(ii) radial momentum

$$\frac{\partial(ru^2)}{\partial r} + \frac{\partial(ruv)}{\partial y} = -r\frac{\partial P}{\partial r} + Pr\left[\frac{\partial}{\partial r}\left(r\frac{\partial u}{\partial r}\right) + \frac{\partial}{\partial y}\left(r\frac{\partial u}{\partial y}\right)\right] - Pr\frac{2u}{r} \quad (11b)$$

(iii) axial momentum

$$\frac{\partial(ruv)}{\partial r} + \frac{\partial(rv^2)}{\partial y} = -r\frac{\partial P}{\partial y} + Pr\left[\frac{\partial}{\partial r}\left(r\frac{\partial v}{\partial r}\right) + \frac{\partial}{\partial y}\left(r\frac{\partial v}{\partial y}\right)\right] + r\,Ra\,Pr\,T \quad (11c)$$

(iv) energy

$$\frac{\partial(ruT)}{\partial r} + \frac{\partial(rvT)}{\partial y} = \left[\frac{\partial}{\partial r}\left(r\frac{\partial T}{\partial r}\right) + \frac{\partial}{\partial y}\left(r\frac{\partial T}{\partial y}\right)\right] \quad (11d)$$

where Pr is the Prandtl number and Ra is the Rayleigh number defined as:

$$Pr = \frac{\nu}{\alpha} \quad (11e)$$

$$Ra = \frac{g\beta\Delta T r_b^3}{\nu\alpha} \quad (11f)$$

and the italics denote the non-dimensional variables. Here u and v are the velocity components in the radial and axial directions, respectively. The Boussinnesq approximation is employed wherein density variations are neglected in the governing equations except the body force terms due to buoyancy, in the momentum equations. Only the right half of the domain is considered in the calculation procedure and symmetry boundary conditions are applied at the centerline. The associated boundary conditions are listed below in non-dimensional form:

symmetry

$$\text{at } r = 0, \quad u = \frac{\partial v}{\partial r} = \frac{\partial T}{\partial r} = 0 \quad (12a)$$

top and bottom boundaries

$$\text{at } y = 0 \text{ and } 1\ T = 0, \quad u = v = 0. \quad (12b)$$

At the free surface, $r = f(y)$:

(i) heat flux through the free surface (dimensionless),

$$\mathbf{q} = \nabla T \cdot \hat{n} \quad (12c)$$

which equals the normal derivative of the temperature at the free surface, and $\hat{n}$ is the unit normal vector to the free surface;

(ii) Marangoni effect,

$$\nabla(\mathbf{V} \cdot \hat{t}) \cdot \hat{n} = Ma \nabla T \cdot \hat{t} \quad (12d)$$

where the shear stress equals the surface tension gradient and gives rise to the normal derivative of the tangential velocity at the free surface. $\mathbf{V}$ is the velocity vector and $\hat{t}$ is the unit tangent vector to the free surface;

(iii) kinematic condition at the free surface

$$\mathbf{V} \cdot \hat{n} = 0 \quad (12e)$$

specifies a no-penetration condition at the free surface.

4. RESULTS AND DISCUSSION

4.1. *Prediction of meniscus shapes*

Meniscus profiles were obtained by solving the Young–Laplace equation in cylindrical coordinates subject to the boundary conditions of fixed radius at the bottom and either (I) fixed contact angle at the top, or (II) fixed volume of the liquid bridge (half domain assuming axial symmetry).

4.1.1. *Low bond number cases.* Initial calculations were conducted following the model proposed by Shyy *et al.* [1] and compared with experimental data provided by Dreeben *et al.* [28]. The parameters were as follows: $r_b = 242$ μm, $Bo = 2.825 \times 10^{-3}$, $AR = 2.24$, contact angle, $\phi_c = 115$ deg and pressurization, $\Delta P = 4.35\%$ of the ambient pressure given by $P_{ambient} = 1.0 \times 10^5$ N m^{-2}. Here r_b is the radius of the feed rod and it is assumed that the meniscus profile is pinned to the edge of the feed rod. It may be noted from the photographs of floating zones provided in ref. [28] that the contact angle is not constant over the contact line, nor is the liquid bridge axisymmetric. The solid–liquid interface is curved and not flat, as is assumed in the simplified model used in the present calculations. It may also be noted that the variation of surface tension with temperature is also

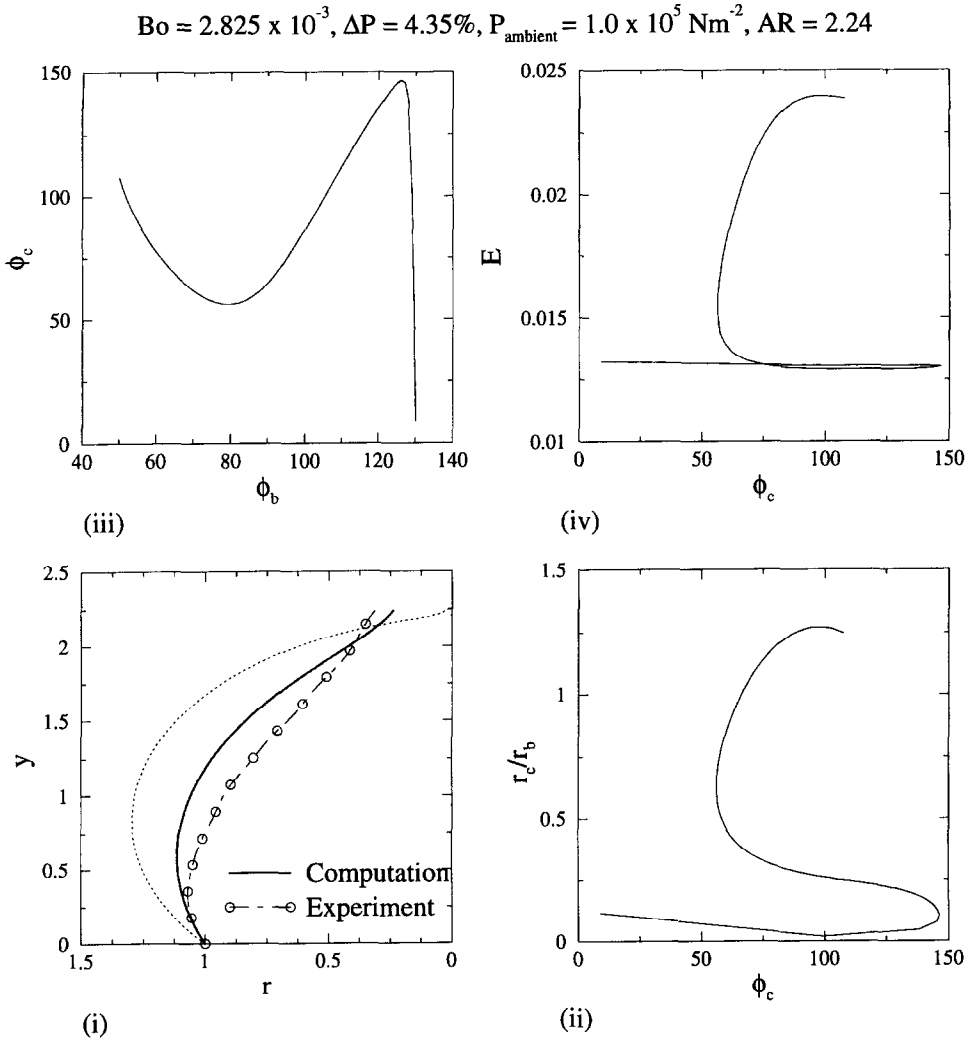

Fig. 2. Comparison of calculated meniscus shapes with the experimental data of Dreeben *et al.* [28]. (i) Calculated and experimentally obtained profiles. It may be observed that two solutions are obtained with the given contact angle of 115°. The profile with the lower free energy matches the experimentally observed profile closely. (ii) r_c vs ϕ_c. (iii) E vs ϕ_c. (iv) ϕ_c vs ϕ_b. The discrepancy between the observed and the calculated results comes from the non-axisymmetry of the experimentally observed profile, the variation of the contact angle along the contact line and curved solid–liquid boundaries.

not considered in this model. The material under consideration is sapphire (Al_2O_3). Figure 2 shows the meniscus profiles obtained using the theoretical model as well as the experimental data.

In Fig. 2, (i) shows the actual profiles obtained by integrating the Young–Laplace equation, that satisfy the imposed contact angle condition at the top, (ii) shows the r_c vs ϕ_c, (iii) shows ϕ_c vs ϕ_b and (iv) is the free energy curve, E vs ϕ_c. In (i), the experimental data from ref. [28] is shown alongside for comparison purposes. (ii) and (iii) show the range of solutions which may be obtained from the Young–Laplace equation. It is obvious that there are two solutions satisfying the given contact angle condition. The profile that minimizes the free energy is shown with a solid line and it matches the experimentally observed profile closely.

A sensitivity study has been conducted to study the formation and physical realizability of the meniscus profiles subject to various boundary conditions and parameters. First, holding the Bond number constant, the aspect ratio was varied over the range $0.5 \leqslant AR \leqslant 2.25$. Figure 3(a) shows the profile shapes at each aspect ratio. Multiple solutions may exist, especially at lower aspect ratios. Only the profiles having the lower free energy are shown.

With a set pull rate and heater power, at steady state, the float zone occupies a prescribed volume. Hence it is useful to examine the solution characteristics subject to the constraint of a fixed volume.

However, in reality, the change in heat transfer characteristics due to the coupling between the movement of the float zone and heat transfer due to conduction as well as buoyancy driven flow, may result in changes of the prescribed melt volume with time. Furthermore, the issue of viewing the static contact angle as a material property needs to be addressed also.

Figure 3(b) displays free energy curves at selected aspect ratios. It may be seen that all the selected curves, except the case of $AR = 1.75$, show a local minimum at $\phi_0 = 115°$. The profile shown at $AR = 1.75$ cannot achieve static stability for the specified contact angle. It is interesting to observe that such a 'window' of AR exists within which, although the menisci exist mathematically, they are not physically realizable. Above and below this 'window' statically stable menisci exist.

4.1.2. *Higher bond number cases.* In practice, the geometrical configurations employed result in a higher value of the Bond number. In particular, we are interested in the following configuration. Given a feed rod diameter of 25 mm [18], and a surface tension of 0.69 N m^{-1} for Al_2O_3, and 1.35 N m^{-1} for NiAl [29], the Bond numbers are 7.6 and 5.7, respectively. Thus the Bond numbers lie in the range 5–10.

The meniscus shape is substantially influenced by the value of ΔP, pressurization, in equation (1). In literature, the value of the pressurization is usually determined by satisfying a constant volume criterion in addition to the boundary conditions imposed. In the present calculations, the objective was to, instead, find a range of pressurization values for which aspect ratios close to unity can be achieved. For a Bond number of 8.8, which was selected in order to effect a comparison with the results of Quon *et al.* [30], it was found that aspect ratios of unity could only be achieved in the range $0.2 \leqslant \Delta P \leqslant 0.3$. The pressurization ranges obtained here are used to generate the subsequent solutions.

Calculations were carried out for aspect ratio of unity, Bond number of 8.8 and six values of pressurization in the range, $0.2 \leqslant \Delta P \leqslant 0.3$. Figures 4 and 5 show the results of the calculations.

Figure 4 shows the profiles and the corresponding free energy curves that are obtained when contact angles of 30 and 60° are imposed. The free energy curves also indicate the range of contact angles for which the Young–Laplace equation can be integrated. It is useful to draw attention to the case of $\phi_0 = 30°$, $\Delta P = 0.2295\%$. It may be observed that two profiles are obtained, marked in Fig. 4(i) with the solid curves, one of them also marked with '○'. The corresponding free energy curve in Fig. 4(iii) is marked with '□' and shows that two solutions can be obtained, one of which satisfies a local minimum. In Fig. 4(i), the unmarked solid curve satisfies a local minimum, indicating static stability. For $\phi_0 = 60°$, none of the obtained profiles satisfy a local minimum.

Figure 5 shows profiles that (i) meet a fixed radius, r_c, condition for three values of $r_c/r_b = 1.0$, 0.75 and 0.5, and (ii) meet a fixed volume constraint of $V = 2$ and 3 (non-dimensionalized). The corresponding r_c vs ϕ_c and V vs ϕ_c show the overall range over which the Young–Laplace equation can be integrated. It may also be noted that the overall solution behavior does not show any abrupt changes as the pressurization, ΔP, is varied over the specified range. Hence, the curves shown in Fig. 5(iv) help in determining the existence of solutions that can simultaneously satisfy a given contact angle condition and a fixed volume. The free energy curves, such as those shown in Fig. 4(iii), show whether the calculated profiles shapes are statically stable.

4.2. *Heat transfer calculations*

A series of calculations were carried out with the geometry of the free surface being determined by the case of $Bo = 8.8$, $\Delta P = 0.2\%$, aspect ratio of unity and with $r_c = r_b$ as shown in Figure 5. The material selected for simulation has the composition Ni_2Al_3. The thermophysical properties of this material are listed in the table below.

Then, recalling that phase change effects are not being considered, if the power input from the heater is 2.3×10^6 W m^{-2}, then the temperature scale can be obtained from equation (8b) as $\Delta T = 36.5$K. For the length scale defined by $r_b = 1.25 \times 10^{-2}$ m, as in the previous calculations for the meniscus shape, this temperature scale implies a Marangoni number of 10^3, a Grashof number of 520 and a Prandtl number of 0.04. These values may vary with the composition of the NiAl, nevertheless, it appears that for the length scales under consideration, thermocapillary convection plays a dominant role in the heat transfer process. In this study, a range of non-dimensional parameters,

$$0 \leqslant Gr \leqslant 10^6 \quad 0 \leqslant Ma \leqslant 10^3 \quad \text{and} \quad Pr = 0.04,\ 0.1$$

have been considered for investigation.

4.2.1. *Numerical procedure.* The governing equation (11) is solved using a pressure-correction type of semi-implicit finite volume formulation in non-orthogonal body-fitted coordinates as described in ref. [2]. In this solution procedure, the Navier–Stokes equations and

Table 1. Thermophysical properties of NiAl and process parameters.

Density	6000 kg m^{-3}
Thermal conductivity	80 W m^{-1} K^{-1}
Heat capacity	586 J kg^{-1} K^{-1}
Coefficient of thermal expansion	1.51×10^{-5} K^{-1}
Kinematic viscosity	9×10^{-7} m^2 s^{-1}
Surface tension coefficient	-2.7×10^{-4} N m^{-1} K^{-1}
Surface tension	1.35 N m^{-1}
Latent heat	5.1×10^5 J kg^{-1}
Melting point	1900 K
Gravitational acceleration	-9.81 m s^{-2}

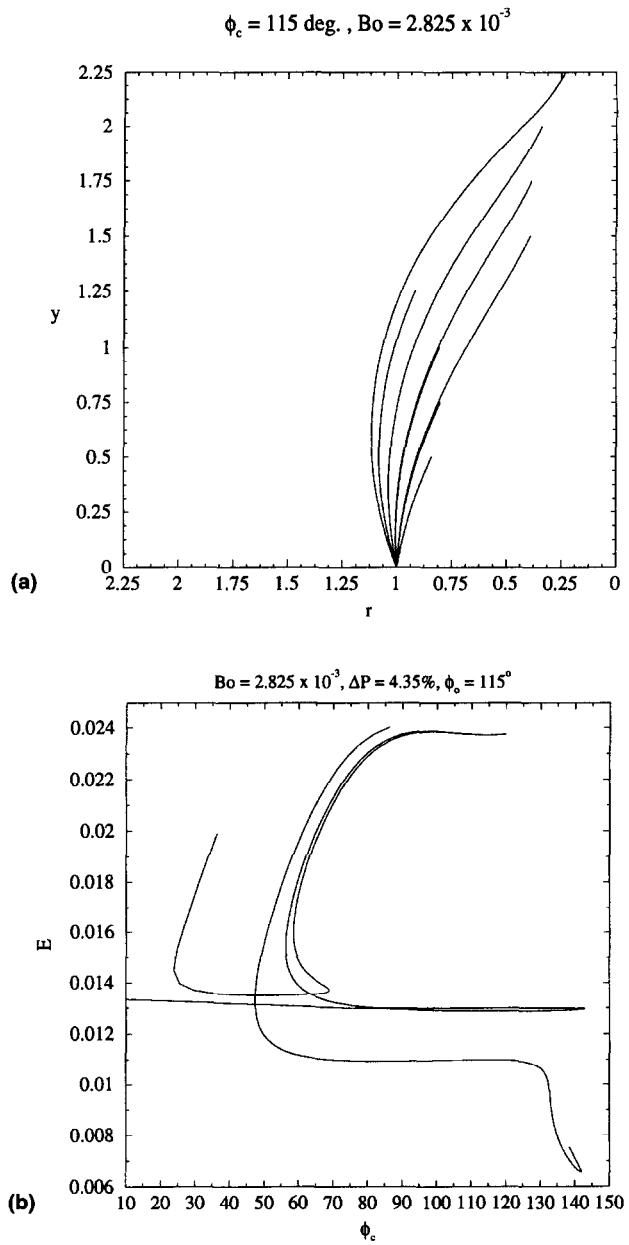

Fig. 3. Meniscus profiles and assessment of physical realizability based on free energy for contact angle of 115°, $Bo = 2.825 \times 10^{-3}$ and $0.5 \leqslant AR \leqslant 2.25$. (a) Meniscus profiles with the lower free energy. (b) Energy versus ϕ_c curves for selected aspect ratios. It may be noted that at $AR = 1.75$, the free energy curve shows a local maximum and hence cannot be statically stable. All other curves display a local minimum, indicating static stability.

the energy equation are integrated over the finite volume, with the fluxes computed numerically by appropriate choice of finite differences. The solution strategy employs a pressure-based algorithm [2, 31] wherein each field equation is solved for in an iterative manner along with a pressure correction equation to ensure that the velocity variables satisfy mass conservation. The convection and the diffusion terms in both the momentum and the energy equations are discretized using second order central differences. A body-fitted coordinate system was generated over the right half of the geometry shown in Fig. 1(b) using transfinite interpolation. The grid points were clustered towards the free surface and for the computations involving Marangoni convection, the grid points were also clustered towards the lower boundary at $y = 0$. For the cases involving only natural convection, two grid systems involving 81×52 nodes and

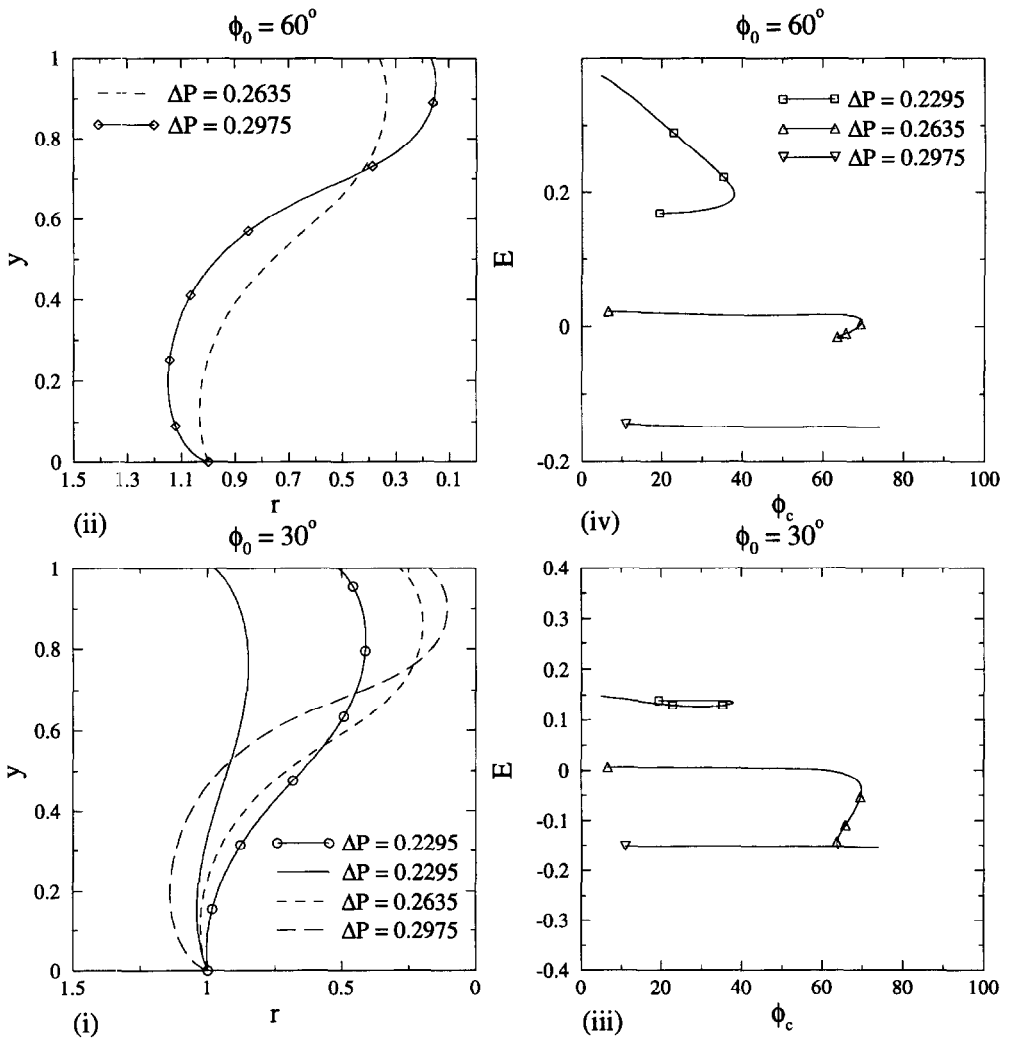

Fig. 4. Calculations for Bond number of 8.8, unity aspect ratio and imposed contact angle condition. (i) and (ii) Profiles meeting a desired contact condition of 30° and 60° respectively. (iii) and (iv) Free energy curves for imposed contact angles of 30° and 60° respectively, for the various values of the pressurization considered. The curves in (iii) and (iv) use the same convention to indicate the pressurization value. (iii) and (iv) also indicate the range of values of ϕ_c which are obtainable by integrating the Young–Laplace equation. It may be noted that for $\phi_0 = 30°$, and $\Delta P = 0.2295\%$, there are two profiles satisfying the given contact condition, indicated by the solid curves. The profile marked with ○ does not minimize the free energy whereas the unmarked one does. None of the other profiles correspond to a local minimum, indicating that, although they mathematically satisfy the Young–Laplace equation, they are not statically stable.

161 × 103 nodes, respectively, were used to discretize the domain. The solutions are indistinguishable, indicating grid independence. The solutions presented are based on the grid system involving 161 × 103 nodes for cases not involving Marangoni convection and 401 × 201 nodes for cases involving Marangoni convection.

4.2.2. *Pure conduction case.* A calculation was carried out with the heat transfer taking place through conduction effects only. The purpose was to carry out an *a posteriori* verification of the temperature scales used to define the Grashof and the Marangoni numbers in subsequent calculations. It may be noted that due to the curved geometry of the free surface, the location of the maximum temperature shifts towards the convex portion of the free surface, as is evident from Fig. 6(a). It is noted that the nondimensional value of T_{max} is 2.3 based on the temperature scale defined in equation (8b).

4.2.3. *Natural convection only.* Figure 6(b) shows the results of incorporating the effects of buoyancy induced convection with a Grashof number of 10^6 and a Prandtl number of 0.1. The streamline pattern shows a single recirculating zone in each half of the domain

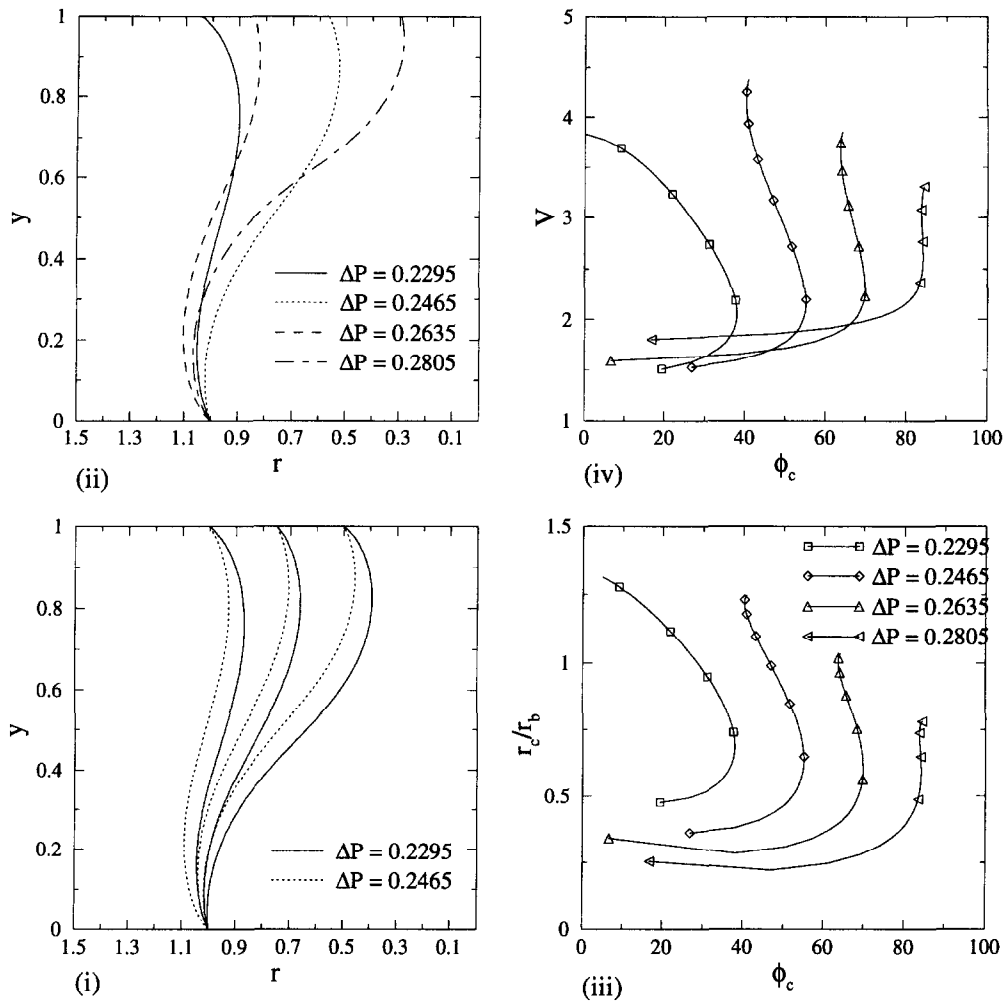

Fig. 5. Calculations for Bond number of 8.8, unity aspect ratio and either (a) imposed radius at the top, or (b) imposed volume of the melt. (i) Fixed r_c and (ii) fixed volume. (iii) r_c/r_b versus ϕ_c and (iv) volume versus ϕ_c curves. The curves in (iii) and (iv) use the same convention to indicate the pressurization value. (iii) and (iv) also indicate the range of values of ϕ_c which are obtainable by integrating the Young–Laplace equation.

and is tangential to the free surface. It may be recalled that since surface tension effects have not been accounted for, the free surface does not exert a shear stress on the fluid. The fluid adjacent to the free surface is heated and rises to the top of the domain due to buoyancy effects, causing the isotherms to be distorted towards the top of the domain and the location of T_{max} to correspondingly shift upwards. The magnitude of T_{max} drops to 1.14, reflecting the validity of the temperature scale defined by equation (8b).

4.2.4. *Interaction of buoyancy driven and Marangoni convection.* (a) $Gr = 10^6$, $Pr = 0.1$ and $Ma = 500$. Figure 7(a) shows the streamfunction and isotherms by imposing a Marangoni number of 500. Since the surface tension decreases with temperature, the tendency of the surface tension gradient-induced shear stress is to reduce the convection strength in the vicinity of the convex part of the free surface and increase the convection strength near the upper part of the domain where the free surface is concave. The overall effect is to marginally shift the location of T_{max} in the downward direction, towards the convex portion of the free surface.

(b) $Gr = 10^6$, $Pr = 0.1$ and $Ma = 1000$. Figure 7(b) shows the effect of increasing the Marangoni number. The trends established in the previous case continue, shifting the location of T_{max} downwards towards the convex portion of the free surface. Since the convection strength in the vicinity of T_{max} is further reduced, the value of T_{max} also increases.

(c) $Gr = 2000$, $Pr = 0.1$ and $Ma = 1000$. Figure 7(c) shows the effect of decreasing the relative strength of buoyancy-induced convection vs Marangoni convection. In this case, the convection pattern is domi-

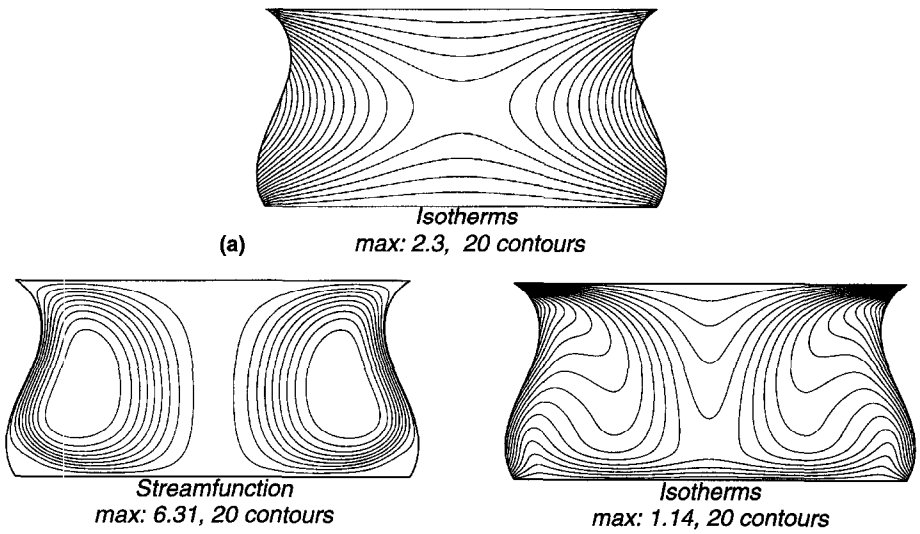

Fig. 6. Effect of natural convection on heat transfer in the float zone. (a) Conduction case. The location of maximum temperature, T_{max}, indicates the effect of boundary curvature. (b) $Gr = 10^6$ and $Pr = 0.1$. Buoyancy driven convection reduces the maximum temperature and shifts its location upwards, following the direction of the velocity field at the boundary. The notable feature is a single counterclockwise rotating convection roll whose spatial extent is of the order of the dimensions of the melt region.

nated by the Marangoni effect. The convection pattern consists of counter-clockwise rotating convection rolls at the top right and the bottom left of the melt adjacent to the free surface and clockwise rotating convection rolls at the bottom right and the top left of the domain. The convection rolls adjacent to the convex portion of the free surface, which occurs at the lower portion of the boundary, are substantially stronger because of the stronger temperature gradients along the convex portion of the free surface. The location of T_{max} is close to that of the pure conduction solution as compared to the high Gr cases. The effect of Marangoni convection is to shift the location of T_{max} to the convex portion of the boundary.

(d) $Gr = 2000$, $Pr = 0.04$ and $Ma = 1000$. Figure 8 shows the effect of decreasing the Prandtl number. The effect of lower Prandtl number is to increase the effective Reynolds number of the flow [2] by decreasing the magnitude of the viscous terms in the momentum equations. The convection pattern is qualitatively similar to the case shown in Fig. 7(c). It may be observed that the isotherms are distorted near the convex portion of the free surface, due to the strong fluid convection, whereas in the upper portion of the domain the pattern resembles the pure conduction case.

From the above cases, some useful inferences can be made that are directly applicable to the float zone growth of NiAl. For the length scales of current experimental interest, it is observed that the pure conduction model of heat transfer is inadequate. Strong convective heat transfer effects may be observed dominated by the Marangoni effect. The Marangoni effect causes clockwise recirculating convection rolls in the bottom right and top left of the domain and counterclockwise recirculating rolls at the top right and bottom left of the domain. For the high Bond numbers that prevail under 1-g conditions on Earth, the free surface has a convex shape in the lower portion of the melt due to the hydrostatic pressure of the melt column. This convex shape induces asymmetry in the shape, spatial extent and strength of the convection rolls and the distribution of the temperature. For the pure conduction case, the convex shape causes the location of the maximum temperature to be shifted towards the convex side of the free surface. In the presence of Marangoni convection, this effect is augmented by the strong convective effect near the convex portion of the domain, due to the stronger temperature gradients along the convex portion of the free surface. This convection in turn causes the location of the maximum temperature to move further downwards. The Marangoni convection completely overwhelms the buoyancy-driven convection for this particular configuration and material properties, augmenting the buoyancy effect in the upper portion of the domain and counteracting it in the lower portion of the domain. Thus the dependence of surface tension on temperature plays a dominant role in the heat transfer characteristics in the float zone.

4.3. *Effect of convection on the meniscus shape*

The deformation of the free surface due to thermocapillary convection is dominated by the capillary number. For example, Zebib *et al.* [3] have found that, whereas the shape is qualitatively sensitive to the Prandtl number, the magnitude of the deformation is determined, to the leading order, by the capillary

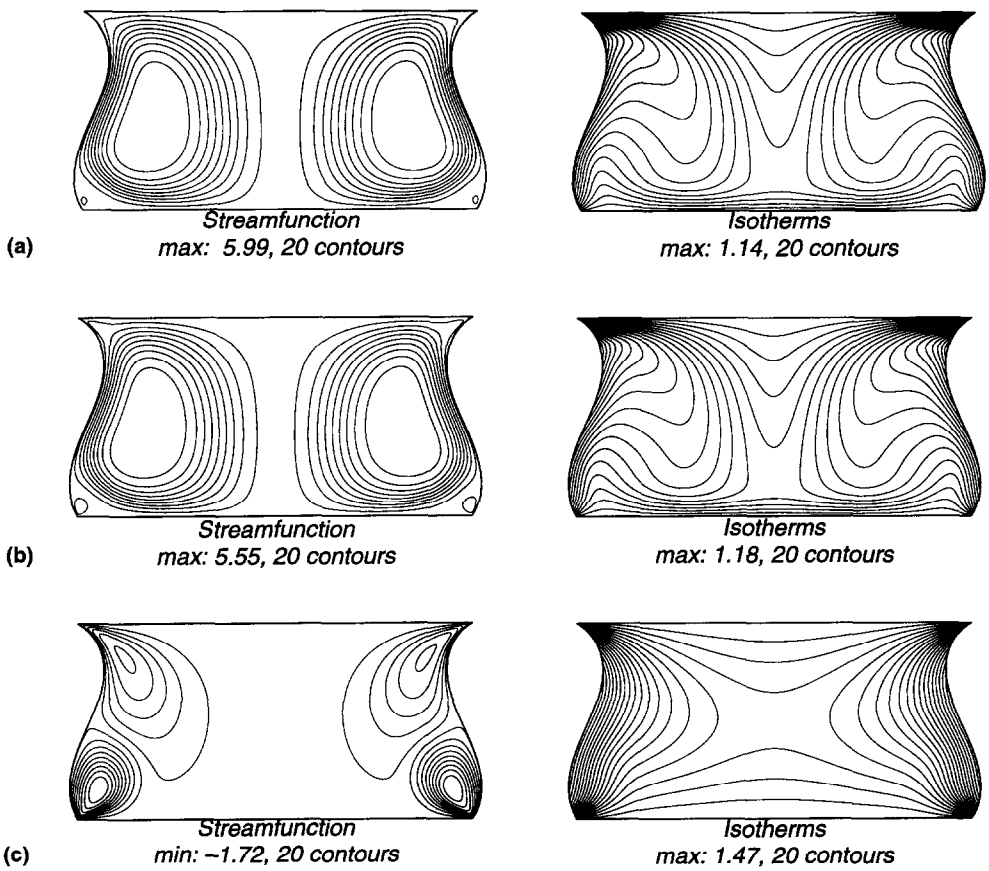

Fig. 7. Effect of Rayleigh and Marangoni number on transport characteristics for a Prandtl number of 0.1. (a) $Gr = 10^6$ and $Ma = 500$. The onset of surface tension driven convection marginally decreases the overall convection strength and marginally shifts the location of T_{max} in the negative z direction. The tendency of the surface tension gradient is to induce a clockwise convection roll in the lower portion of the domain and a counterclockwise roll in the upper portion of the domain, the spatial extent of which is confined to the region adjacent to the free boundary compared with the case of buoyancy driven convection. (b) $Gr = 10^6$ and $Ma = 1000$. Strong surface tension effects cause the overall convection strength to decrease and T_{max} to increase and shift further in the downwards in the negative z direction. The tendency of the surface tension gradient is to induce a clockwise convection roll in the lower portion of the domain and a counterclockwise roll in the upper portion of the domain. (c) $Gr = 2000$, and $Ma = 1000$. With decreasing Grashof number, the lower clockwise rotating convection cell due to the Marangoni effect becomes more evident. The location of the maximum temperature shifts downward because of the convex shape of the lower part of the free surface. As a result, the convection in the upper and central regions is substantially weaker than the cases dominated by buoyancy induced convection.

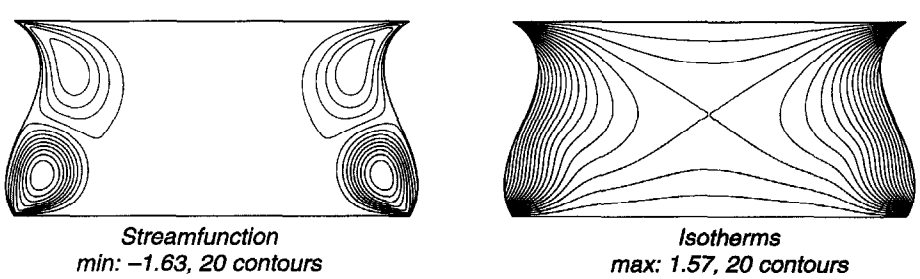

Fig. 8. Effect of natural convection and Marangoni convection for a Prandtl number of 0.04. $Gr = 2000$ and $Ma = 1000$.

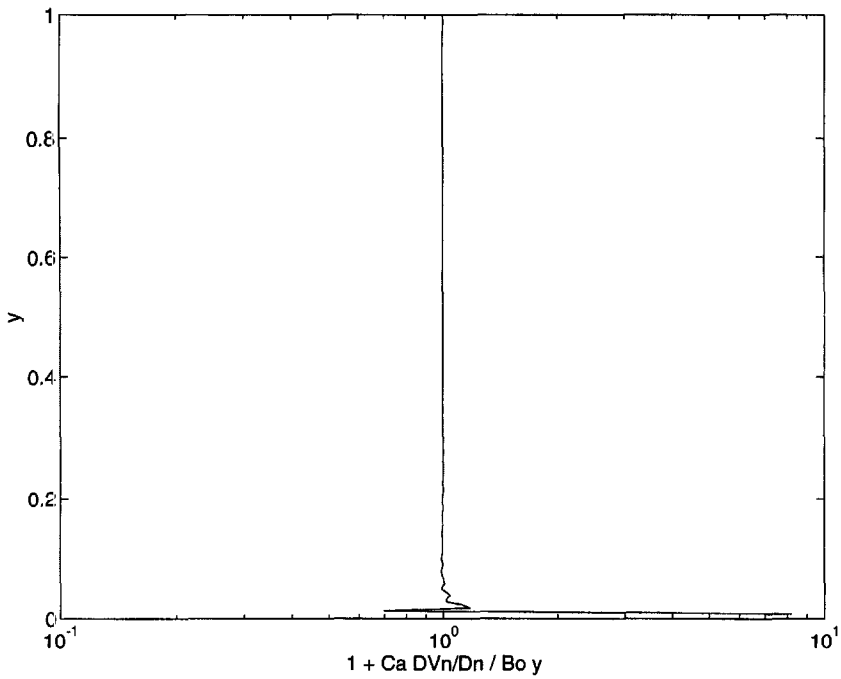

Fig. 9. Semilog plot of y vs $1+(Ca\,\partial V_n/\partial n)/(Bo\,y)$ to show the locations where the normal stress term due to convection becomes important compared to the hydrostatic pressure.

number. Equation (7) describes the role of the normal stress due to the normal derivative of the normal velocity component at the free surface in changing the shape of the meniscus. Under 1-g conditions and at the length scales considered, the hydrostatic terms described by the high Bond numbers are the dominant terms in equation (7) and the normal stress terms due to convection are small compared to the hydrostatic term. The Bond number for this case is $Bo = 8.8$ and the capillary number, $Ca = 1.5 \times 10^{-5}$. The impact on the surface curvature varies with the vertical distance and is described by

$$1+\frac{Ca\,\partial V_n/\partial n}{Bo\,y}.$$

This quantity may be plotted to show the variation of its magnitude along the y-axis as shown in Fig. 9. This shows that, except at the lowermost corners of the domain, the normal stress term is vanishingly small. Considering that the meniscus is pinned at both the top and the bottom of the domain, the correction to the overall shape of the meniscus is expected to be modest except at the lowermost corner where the curvature will be substantially lower. Since the effect is extremely localized at the corner locations where the flow turns to match the boundary, the overall effect on the heat transfer and convection characteristics is expected to be negligible for this case. Accordingly, corrections to the meniscus shape appear unnecessary in this particular study. It is also to be observed that the percentage variation of the surface tension with temperature is less than 1% and hence cannot significantly affect the force balance at the interface.

5. CONCLUSION

Computational studies have been carried out to assess the computed meniscus shapes based on the concept of free energy [1]. It is noted that as the Bond number is increased the number of available solutions drops sharply. With a given Bond number, a window of AR may exist, within which menisci may exist mathematically, but are not physically realizable because they are not statically stable. Above and below this window, menisci are again statically stable. The physical realizability of the meniscus profiles is sharply affected by the material properties such as surface tension and density through the Bond number, and the geometry through the Bond number and aspect ratio. However, the mathematical boundary conditions imposed have less impact on the meniscus profiles.

Having demonstrated the viability of the calculation procedure by comparison with experimental data, the procedure was applied to Bond numbers and geometrical parameters that are typical of float zone processes. Neglecting temperature variations and dynamical effects it is shown that static stability of the meniscus is much more difficult to achieve at high Bond numbers and high aspect ratios. Even though the Young–Laplace equation can be integrated to obtain meniscus profiles, many of these profiles fail

to satisfy the free energy minimum showing that the profiles are not statically stable.

Heat transfer studies were carried out on the melt configuration described by the meniscus shape of $AR = 1$ and a Bond number of 8.8 with the ends pinned to fixed radius values. The material properties of particular interest here are those of NiAl. It was found that, at the length scales of interest, the convective effects due to the surface tension gradient are substantially more important than that due to buoyancy driven convection. Also, the normal stress due to convective effects and the variation of surface tension with temperature are found to be insignificant in perturbing the meniscus shape from the static equilibrium position except at the corner regions where the streamlines turn to accommodate the abrupt change in geometry. However, this effect is extremely localized to the vicinity of the corners where the meniscus contacts the solid. If the meniscus is pinned to the solid, then the normal stress due to the turning of the streamlines impacts the meniscus through the curvature and its effects on the overall shape may be expected to be negligible. It is found that as the strength of thermocapillary convection increases, it interacts with the complex geometry defined by the curved meniscus shape, to increase the convection strength in the vicinity of the convex part of the free surface and reduce it in the part of the domain where the boundary shape is concave. The above effect is mainly due to the fact that only the heat flux is prescribed at the meniscus and consequently the location of the maximum temperature is free to move to accommodate the local convection which has a substantial impact on the surface tension gradient at the boundary. The results reported here are directly relevant to the float zone crystal growth technique.

Acknowledgement—Some of the calculations were carried out on a Cray Y-MP at Army Corps of Engineers, WES Supercomputer Center at Vicksburg, Mississippi. Partial support from AFOSR University Research Initiative and helpful discussion with Professors Reza Abbaschian and Michael Kaufman of University of Florida, are gratefully acknowledged.

REFERENCES

1. W. Shyy, H. S. Udaykumar and S.-J. Liang, Quasi-equilibrium meniscus formation with hysteresis effects, *Phys. Fluids A* **5**(11), 2610–2623 (1993).
2. W. Shyy, *Computational Modeling for Fluid Flow and Interfacial Transport*. Elsevier, Amsterdam (1994).
3. A. Zebib, G. M. Hornsy and E. Meiburg, High Marangoni number convection in a square cavity, *Phys. Fluids A* **28**(12), 3467–3476 (1985).
4. B. M. Carpenter and G. M. Homsy, Combined buoyant thermocapillary flow in a cavity, *J. Fluid Mech.* **207**, 121–132 (1989).
5. B. M. Carpenter and G. M. Homsy, High Marangoni number convection in a square cavity: part II, *Phys. Fluids A* **2**(2), 137–149 (1990).
6. W. Shyy and M. -H. Chen, A study of buoyancy induced and thermocapillary flow of molten alloy, *Comput. Meth. Appl. Mech. Engng* **105**, 333–358 (1993).
7. W. Shyy and M.-H. Chen, Interaction of thermocapillary and natural convection flows during solidification: normal and reduced gravity conditions, *J. Crystal Growth* **108**, 247–261 (1991).
8. W. Shyy and M.-H. Chen, Double-diffusive flow in enclosures, *Phys. Fluids A* **3**, 2592–2607 (1991).
9. T. J. McNeil, R. Cole and R. S. Subramanian, Surface tension driven flow in a glass melt, *J. Am. Ceram. Soc.* **68**(5), 254–259 (1985).
10. N. Kobayashi, Computer simulation of the steady flow in a cylindrical floating zone under low gravity, *J. Crystal Growth* **66**, 63–72 (1984).
11. N. Kobayashi, Steady convection caused by the temperature inhomogeneity in a cylindrical floating zone, *Jap. J. Appl. Phys.* **27**(1), 20–24 (1988).
12. J. Y. Murthy, A numerical simulation of flow, heat and mass transfer in a floating zone at high rotational Reynolds numbers, *J. Crystal Growth* **83**, 23–34 (1987).
13. K. H. Lie, D. N. Riahi and J. S. Walker, Buoyancy and surface tension driven flows in float zone crystal growth with a strong axial magnetic field, *Int. J. Heat Mass. Transfer* **32**(12), 2409–2420 (1989).
14. G. P. Neitzel, J. R. Hyer and D. F. Jankowski, Thermocapillary convection in a model float zone, AIAA Paper No. AIAA-90-0406 (1990).
15. J. Li, J. Sun and Z. Saghir, Buoyant and thermocapillary flow in liquid encapsulated floating zone, *J. Crystal Growth* **131**, 83–96 (1993).
16. J. Li and M. Z. Saghir, Coupled buoyant and surface tension driven convection in liquid encapsulation floating zone under 1-*g* and 0-*g* with deformable interfaces, AIAA Paper No. AIAA-94-0793 (1994).
17. Y. Zhang and J. I. D. Alexander, Surface tension and buoyancy driven flow in a non-isothermal liquid bridge, *Int. J. Numer. Meth. Engng* **14**, 197–215 (1992).
18. R. Abbaschian, A. Gokhale, E. Jensen and R. Panchapakesan, Liquid encapsulated molten zone (LEMZ) processing on STS-57, AIAA 94–0563 (1994).
19. R. Finn, *Equilibrium Capillary Surfaces*. Springer, New York (1986).
20. A. D. Myshkis, V. G. Babskii, N. D. Kopachevskii, L. A. Slobozhanin and A. D. Tyuptsov, *Low Gravity Fluid Mechanics* (Translated by R. S. Wadhwa). Springer, New York (1987).
21. P. Concus, Capillary surfaces in microgravity. In *Low-Gravity Fluid Dynamics and Transport Phenomena* (Edited by J. N. Koster and R. L. Sani), Vol. 130, pp. 183–206. Progress in Astronautics and Aeronautics. AIAA, Washington, DC (1990).
22. S. R. Coriell, S. C. Hardy and M. R. Cordes, Stability of liquid zones, *J. Colloid. Interface Sci.* **60**(3), 126–136 (1977).
23. D. N. Riahi and J. S. Walker, Float zone shape and stability with the electromagnetic body force due to a radio-frequency induction coil, *J. Crystal Growth*, **94**, 635–642 (1989).
24. D. Langbein, Oscillations of finite liquid columns, *Microgravity. Sci. Technol.* **V/2**, 73–85 (1992).
25. J. A. Tsamopoulos, A. J. Poslinski and M. E. Ryan, Equilibrium shapes and stability of captive annular menisci, *J. Fluid Mech.* **197**, 523–549 (1988).
26. J. A. Tsamopoulos, T. -Y. Chen and A. Borkar, Viscous oscillations of capillary bridges, *J. Fluid Mech.* **235**, 579–609 (1992).
27. C. Huh and S. G. Mason, Effects of surface roughness on wetting, *J. Colloid. Interface Sci.* **60**(3), 11–38 (1977).
28. A. B. Dreeben, K. M. Kim and A. Schulko, Measurement of meniscus angle in laser heated float zone growth of constant diameter sapphire crystals, *J. Crystal Growth* **50**, 126–132 (1980).
29. B. J. Keene, Review of data for the surface tension of pure metals, *Int. Metals Rev.* **38**, 157–192 (1993).
30. D. H. H. Quon, S. Chehab, J. Aota, A. K. Kurikose,

S. S. B. Wang, M. Z. Saghir and H. L. Chen, Float-zone crystal growth of bismuth germanate and numerical simulation, *J. Crystal Growth* (to be published).
31. S. V. Patankar, *Numerical Heat Transfer and Fluid Flow*. Hemisphere, Washington, DC (1980).
32. W. Shyy, S. S. Tong and S. M. Correa, Numerical recirculating flow calculation using a body-fitted coordinate system, *Numer. Heat Transf.* **8,** 99–113 (1985).
33. W. Shyy and T. C. Vu, On the adoption of velocity variable and grid system for fluid flow computation in curvilinear coordinates, *J. Comput. Phys.* **92,** 82–105 (1991).